ACS APPLIED MATERIALS & INTERFACES

Research Article

www.acsami.org

Facile Fabrication of Hierarchical TiO_2 Nanobelt/ZnO Nanorod Heterogeneous Nanostructure: An Efficient Photoanode for Water Splitting

Kai Pan,*[,†] Youzhen Dong,[†] Wei Zhou,[†] Qingjiang Pan,[†] Ying Xie,[†] Tengfeng Xie,[‡] Guohui Tian,[†] and Guofeng Wang[†]

[†]Key Laboratory of Functional Inorganic Material Chemistry, Ministry of Education, School of Chemistry and Materials Science, Heilongjiang University, Harbin 150080, People's Republic of China

[‡]College of Chemistry, Jilin University, Changchun 130012, People's Republic of China

Supporting Information

ABSTRACT: The TiO_2 nanobelt/ZnO nanorod composite photoelectrodes with flower-like and/or grass-like microstructures have been fabricated via a facile solution growth routine, just by controlling the treatment of the TiO_2 nanobelt substrate. For the flower-like composite, the ZnO nanorods disperse orientationally on TiO_2 nanobelt films, while for the grass-like one, ZnO nanorods grow disorderly like grass on the TiO_2 nanobelt film surface. Furthermore, quasi-Fermi energy level changes of both photoelectrodes have been quantitatively characterized by the surface photovoltage based on the Kelvin probe, which clearly reveals the efficiency of photogenerated electron−hole separation. Owing to the decrease of quasi-Fermi energy level, the flower-like TiO_2 nanobelt/ZnO nanorod heterogeneous nanostructure presents a high efficiency of photogenerated electron−hole separation. Therefore, the flower-like TiO_2 nanobelt/ZnO nanorod heterogeneous nanostructure photoelectrode has achieved a better performance of water splitting compared with the grass-like TiO_2 nanobelt/ZnO nanorod one.

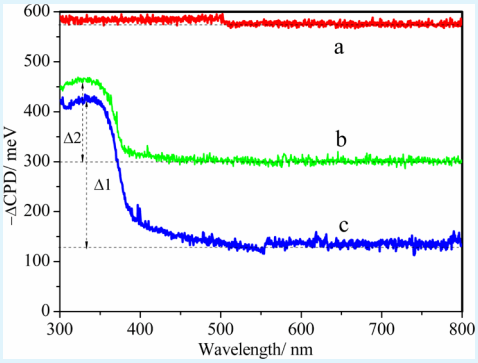

KEYWORDS: *heterogeneous nanostructure, water splitting, electron−hole separation, surface photovoltage, quasi-Fermi energy level*

1. INTRODUCTION

With the tremendous consumption of traditional fossil fuel and the serious environmental pollution, scientists have recently done their best to seek a renewable and clean energy resource. As one of the ideal renewable energy sources, sunlight has already been widely used in manufacturing and human living due to its endless supply without district limit.[1,2] So far, special attention has been focused on the application of sunlight in photoelectrochemical devices. The photoelectrochemical cells (PECs) for water splitting and dye-sensitized solar cells (DSSCs) are two popular photoelectrochemical systems. Although they have different resultant energy-product forms, they possess similar principles and require photoelectrodes made of nanoporous thin films of semiconductor nanocrystals.[3−6] Due to their low cost, easy availability, and excellent physicochemical stability, metal oxide semiconductor nanomaterials have been widely applied as photoelectrode materials in PEC and DSSC devices.[7−9] Many charge-transfer processes such as photoelectrode−electrolyte interfacial exciton separation and electron transport (collection) in the nanoporous photoelectrodes take place; however, the photogenerated electron transport and recombination are generally regarded as predominant factors to determine the performance of PECs and DSSCs.[10,11]

Since the first report about water splitting using a single-crystalline TiO_2 electrode, semiconductor materials have been paid much attention for water splitting into hydrogen energy.[12−15] The conventionally used TiO_2 (or ZnO) photoelectrodes for water splitting are composed of nanoporous nanoparticles.[16−18] For example, S. Han et al. used a layer-by-layer process to prepare a TiO_2 nanoparticle/ZnO nanoparticle composite film. The resultant photoelectrode showed a power conversion efficiency of 0.67% in DSSCs.[19] However, such a nanoparticle system still suffers from many defects such as grain boundaries and surface traps, which resulted in multiple trapping events,[20−24] and this hinders electron transport and eventually decreases the hydrogen generation rate. Recently, some strategies have been developed to optimize the structure of heterogeneous photoelectrodes to promote the performance of PECs. One of them was to replace the nanoparticles with a heterojunction nanocomposite, such as the ZnO−TiO_2 nanoparticle composite, the rutile TiO_2 nanorod−anatase TiO_2 nanoparticle composite, and so on.[25−27] J. Li et al. synthesized the bicomponent anatase TiO_2 nanoparticle/wurtzite ZnO nanorod composite, which exhibited an improved photo-

Received: December 9, 2012
Accepted: August 19, 2013
Published: August 19, 2013

degradation reaction of methyl blue,[25] but there are still lots of electron transfer interfaces among nanoparticles, which are detrimental to photoelectron transport. The other promising strategy was to apply one-dimensional (1D) nanomaterials, such as ZnO nanowires[28−30] and TiO_2 nanotubes,[31−34] as the PEC photoelectrode. This is because these structural materials can significantly improve the electron transport at the photoelectrode/electrolyte interface by providing a direct conduction pathway and reducing the number of interparticle hops. Y. Li et al. fabricated hydrogen-treated TiO_2 nanowire arrays and hematite nanowires, respectively. Both improved the performance of PEC water splitting due to the creation of a high density of oxygen vacancies that serve as electron donors.[35,36] P. Yang et al. reported that the length and surface properties of TiO_2 nanowires could have a dramatic effect on their photoelectrochemical properties. Atomic layer deposition was also used to deposit an epitaxial rutile TiO_2 shell on nanowire electrodes, which enhanced the photocatalytic activity.[35] However, the low electron mobility in 1D nanomaterials can be an obstacle for electron transport along the nanowires to reach the electrical contact.[37,38] Therefore, design and fabrication of novel 1D/1D heterogeneous architectures with hierarchical heterogeneous nanostructures, which possess the rapid electron transport characteristic and decreased defect numbers, are highly demanded to further improve the photocatalytic activity for water splitting. L. Jiang et al. prepared three-dimensional ZnO/TiO_2 hierarchical structures with high densities of secondary ZnO nanostructures grown on primary TiO_2 fibers,[39] but the systematic research about the influence of different morphologies of ZnO/TiO_2 heterostructures on the photocatalytic activity for water splitting is not reported.

In this work, the ZnO nanorods were grafted on TiO_2 nanobelts via a solution growth routine. By controlling the treatment of the TiO_2 nanobelt substrate, the hierarchical flower-like and grass-like TiO_2 nanobelt/ZnO nanorod architectures are prepared, respectively. Electron microscopy images indicate that the better electrical contact is formed in the flower-like TiO_2 nanobelt/ZnO nanorod. Such 1D/1D heterogeneous architectures possess low defect numbers and promote the electron transport. Furthermore, the influence of different morphologies of TiO_2 nanobelt/ZnO nanorod heterogeneous architectures on the photocatalytic activity for water splitting is systematically studied. The water splitting performance results demonstrate that the hierarchical flower-like TiO_2 nanobelt/ZnO nanorod heterogeneous nanostructure photoelectrode exhibits a higher photocurrent compared with the grass-like one. The interfacial electron transport and quasi-Fermi energy level change of hierarchical photoelectrodes have been characterized using the surface photovoltage (SPV) based on Kelvin probe (KP). This work may improve the understanding of the unique properties of hierarchical 1D/1D heterogeneous nanostructures in photoelectrochemistry.

2. EXPERIMENTAL SECTION

2.1. Chemicals. Polyethylenimine (branched, low molecular weight, Aldrich) and commercial TiO_2 powder (Degussa P25, which consists of about 30% rutile and 70% anatase and a particle size of about 20 nm) are purchased from standard sources. All the other solvents and chemicals used in the experiments are at least reagent grade. Unless otherwise noted, all the chemicals are used as received. The transparent conducting glass (TCO, F-doped SnO_2 layer, sheet resistance is 20 Ω/square, Nippon sheet glass, Japan) is used for the electrode substrate. Milli-Q water with a resistivity of 18 MΩ cm^{-1} is used in all the experiments.

2.2. Synthesis of 1D TiO_2 Nanobelts. The TiO_2 nanobelts were synthesized via a facile hydrothermal method based on our previous work.[40] Amounts of 7.2 g of TiO_2 powders (Degussa P25) were first dispersed in 40 mL of 15 M NaOH aqueous solution. After stirring for 1 h, the obtained suspension was transferred into a Teflon-lined stainless steel autoclave. The autoclave was maintained at 170 °C for 72 h and then was cooled to room temperature naturally. The obtained white precipitate was recovered by centrifugation and washed with 0.1 M HCl solution and deionized water several times until pH = 7. Finally, they were dried at 80 °C and calcined at 700 °C for 3 h in air for the phase transition from TiO_2−B into the anatase phase.[41]

2.3. Fabrication of the TiO_2 Nanobelt/ZnO Nanorod Photoelectrode. The flower-like hierarchical TiO_2 nanobelt/ZnO nanorod heterogeneous photoelectrodes were fabricated via the solution growth method (see Chart 1A). First, the 0.55 g TiO_2 nanobelts were ultrasonically dispersed in 50 mL of 5 mM $Zn(Ac)_2{\cdot}2H_2O$ ethanol solution. The resulting white precipitate was recovered by centrifugation and dried at room temperature. Second, the ZnO seed-coated TiO_2 nanobelt pastes were prepared. A doctor-blade technique was used to fabricate the ZnO seed-coated TiO_2 nanobelt film (Chart 1A I). Third, the solution growth of ZnO nanorods occurred (Chart 1A II).[42] ZnO nanorods were grown by immersing ZnO seed-coated TiO_2 nanobelt film in aqueous solutions containing 25 mM zinc nitrate hydrate, 25 mM hexamethylenetetramine, and 5−7 mM polyethylenimine at 92 °C for 2.5 h. Because nanorod growth slowed after this period, substrates were repeatedly immersed into fresh solution baths to obtain long nanorods (total reaction times of up to 10 h). The photoelectrodes were then rinsed with deionized water and baked in air at 400 °C for 30 min. At last, the flower-like hierarchical TiO_2 nanobelt/ZnO nanorod heterogeneous photoelectrodes were obtained.

As a control, the grass-like TiO_2 nanobelt/ZnO nanorod composite photoelectrodes were also fabricated via a similar method (see Chart 1B). First, the TiO_2 nanobelt pastes were prepared and used to fabricate the TiO_2 nanobelt film (Chart 1B 1). Second, a layer of ZnO seeds was adsorbed on the surface of TiO_2 nanobelt films using the dip-coating technique (Chart 1B 2). Third, the solution growth of

Chart 1. Flow Chart for the Fabrication of Flower-Like Hierarchical TiO_2 Nanobelt/ZnO Nanorod Heterogeneous Photoelectrodes (A) and Grass-Like TiO_2 Nanobelt/ZnO Nanorod Composite Photoelectrodes (B)[a]

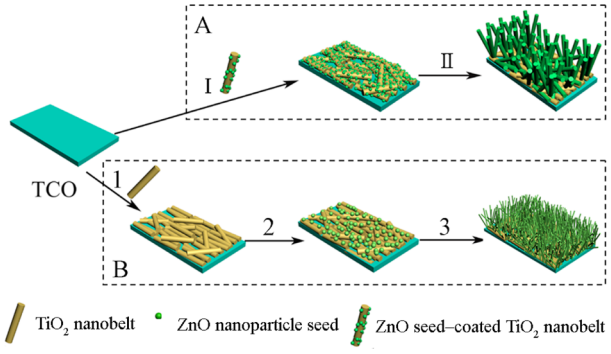

[a]A I: the ZnO seed-coated TiO_2 nanobelt pastes were prepared and used to fabricate the ZnO seed-coated TiO_2 nanobelt film. A II: the flower-like hierarchical TiO_2 nanobelt/ZnO nanorod heterogeneous photoelectrodes, based on the ZnO seed-coated TiO_2 nanobelt film, were obtained via the solution growth method. B 1: the TiO_2 nanobelt pastes were prepared and used to fabricate the TiO_2 nanobelt film. B 2: a layer of ZnO seeds was adsorbed on the surface of TiO_2 nanobelt films using the dip-coating technique. B 3: the grass-like TiO_2 nanobelt/ZnO nanorod photoelectrodes were obtained via the similar ZnO nanorod growth method.

dx.doi.org/10.1021/am402154k | ACS Appl. Mater. Interfaces 2013, 5, 8314−8320

ZnO nanorods occurred on the surface of the TiO_2 nanobelt (Chart 1B 3). It has a similar ZnO nanorod growth method with flower-like hierarchical nanostructure. The naked TiO_2 nanobelt and ZnO nanorod photoelectrodes were also prepared, respectively. All film electrodes were fabricated with 10 μm thickness.

2.4. Characterization. Raman scattering spectra were measured by an HR-800 LabRam confocal Raman microscope with a backscattering configuration made by JY company in France, excited by the 514.5 nm line of an argon ion laser at room temperature. The scanning electron microscopy (SEM) images were taken using a Hitachi S-4800 instrument operating at 15 kV. The transmission electron microscopy (TEM) experiment was performed on a JEM-3010 electron microscope (JEOL, Japan) with an acceleration voltage of 200 kV. Carbon-coated copper grids were used as the sample holders.

The photocatalytic activity of the TiO_2 nanobelt/ZnO nanorod composite nanostructure photoelectrode for water photoelectrolysis was characterized by measuring the photocurrent density under xenon lamp irradiance in 0.5 M Na_2SO_4 electrolyte. Water photoelectrolysis was carried out in a standard three-electrode configuration with a Pt foil counter electrode and a saturated Ag/AgCl reference electrode. The irradiance size of the photoanode was 0.6 cm^2. The photocurrent density/potential ($J-V$) curves and photocurrent density/time ($J-t$) curves at constant potential were recorded on a BAS100B electrochemical potentiostat (Bioanalytical Systems Inc., USA). The irradiance intensity was about 120 mW cm^{-2}.

KP-based SPV measurements were carried out on a commercial KP system (KP Technology Ltd., Scotland, UK). The width of the gold reference probe is 1.8 mm, and its work function is 5.1 eV. The SPV was measured by tracking the change of contact potential difference (ΔCPD) between the sample and the Au probe. The SPV spectra were obtained by scanning the monochromatic light through the visible and UV range with a rate of ca. 30 nm min^{-1}. All the SPV measurements were operated under ambient conditions, and the raw data were not treated further. Constant light intensity at each wavelength was not used in the SPV measurements, and the monochromic light intensity depended on the xenon lamp spectral energy distribution. The largest intensity of the incident monochromatic light is less than 80 μW cm^{-2}.[43,44]

3. RESULTS AND DISCUSSION

3.1. Structural Characterization of Hierarchical TiO_2 Nanobelt/ZnO Nanorod Nanostructures. The TiO_2 nanobelts were synthesized via a facile hydrothermal method. One can see that the TiO_2 nanobelts are 2−4 μm in length and 100−300 nm in width, and nanobelts are randomly dispersed in the TCO substrate because of the doctor blade fabrication (Figure 1a). The naked ZnO NR arrays vertically oriented on the TCO substrate, and its diameter is about 130 nm (Figure 1b). After a layer of ZnO seeds was adsorbed on the surface of TiO_2 nanobelt films using the dip-coating technique, ZnO nanorods grow disorderly like grass on the TiO_2 nanobelt film surface via the solution growth method (Figure 1c). The grass-like TiO_2 nanobelt/ZnO nanorod composite photoelectrode is formed. This is because most ZnO nanorods grow in the space between TiO_2 nanobelts, and only a few ZnO nanorods grow on the surface of TiO_2 nanobelts (Scheme S1 (b), Supporting Information). However, for the flower-like hierarchical TiO_2 nanobelt/ZnO nanorod heterogeneous photoelectrode (Figure 1d), the ZnO nanorods disperse orientationally on TiO_2 NB films with flower-like nanostructure. For the flower-like hierarchical TiO_2 nanobelt/ZnO nanorod composite, the ZnO seeds are uniformly dispersed in the TiO_2 nanobelt via the precoating process, thus the ZnO nanorods can epitaxially grow around the TiO_2 nanobelt. As a result, ZnO nanorods rationally grow, and the flower-like hierarchical TiO_2 nanobelt/ZnO nanorod composite is formed (Scheme S1 (a), Supporting Information). With respect to the grass-like TiO_2 nanobelt/ZnO nanorod composite, TiO_2 nanobelts and ZnO nanorods grow mussily together (Figure 2a). However, some ZnO nanorods grow on the sidewalls of TiO_2 nanobelt backbones with different radial angles (Figure 2b). Both the flower-like and grass-like TiO_2/ZnO hierarchical structures possess good electrical contacts. However, the flower-like TiO_2/ZnO hierarchical structure has a better electrical contact. To exactly investigate the crystal structure of the as-prepared flower-like TiO_2 nanobelt/ZnO nanorod, HRTEM has been performed on this specimen. It could be seen that the composite is well crystallized with lattice fringes of about 0.261 and 0.352 nm, corresponding to an interplanar spacing of the wurtzite ZnO [0001] and anatase TiO_2 (001) crystal plane, respectively. Moreover, the [0001] crystal planes of the wurtzite phase extend into the anatase TiO_2 core (Figure 2c). According to these results, it can be concluded, to a certain extent, that the flower-like hierarchical TiO_2 nanobelt/ZnO nanorod heterogeneous structure possesses the better electrical contact. Such a hierarchical and heterogeneous nanostructure is able to maximize the contact between the photoelectrode and electrolyte and minimize the formation of dangling bonds, large crystallographic discrepancies, and voids in the interface region. This would facilitate interfacial charge transfer.[45]

Raman spectroscopy, having a very sensitive response to the crystallinity and microstructure of materials, is usually used to unambiguously distinguish the local order character of characteristics of TiO_2 and ZnO nanomaterials.[46,47] It can be

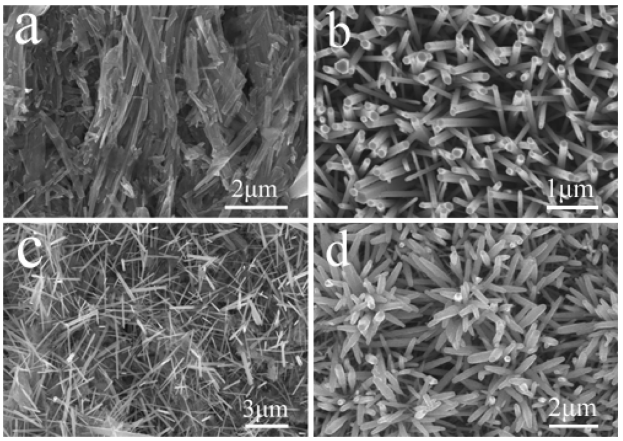

Figure 1. SEM images of the TiO_2 nanobelt photoelectrode (a), ZnO nanorod photoelectrode (b), grass-like TiO_2 nanobelt/ZnO nanorod composite photoelectrode (c), and flower-like hierarchical TiO_2 nanobelt/ZnO nanorod heterogeneous photoelectrodes (d).

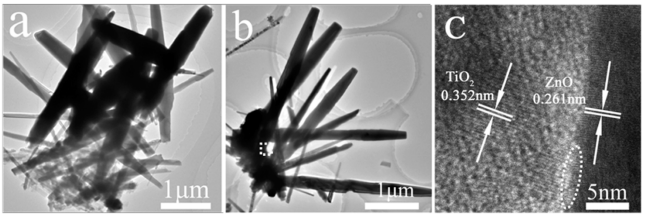

Figure 2. TEM images of the grass-like TiO_2 nanobelt/ZnO nanorod composite (a) and flower-like hierarchical TiO_2 nanobelt/ZnO nanorod heterogeneous nanostructure (b). HRTEM images of flower-like hierarchical TiO_2 nanobelt/ZnO nanorod heterogeneous nanostructures (c).

seen that the remarkable Raman shifts appear at 143, 196, 396, 515, and 633 cm^{-1}, which are related to the E_g, E_g, E_g, B_{1g}, and A_{1g} vibration modes of anatase TiO_2, respectively (Figure 3a).[48]

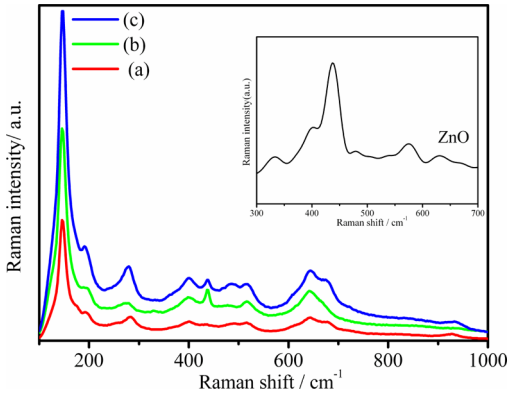

Figure 3. Raman spectra of the TiO_2 nanobelt photoelectrode (a), grass-like TiO_2 nanobelt/ZnO nanorod composite photoelectrode (b), and flower-like hierarchical TiO_2 nanobelt/ZnO nanorod heterogeneous photoelectrode (c). Inset is the Raman spectrum of the ZnO nanorod photoelectrode.

In the case of ZnO nanorods growing on the TiO_2 nanobelt substrate via a solution growth routine, a new Raman shift peak at 437 cm^{-1} appears, which is ascribed to the remarkable E_{2H} mode of hexagonal wurtzite ZnO, besides the Raman shift peaks of anatase TiO_2 (Figure 3b, c).[49] The inset of Figure 3 also shows the Raman shift of ZnO nanorods at 437 cm^{-1}. It indicates that the formed nanostructures are composed of the anatase TiO_2 phase and wurtzite ZnO phase.

Besides the TCO substrate diffraction peaks (Figure 4a), the characteristic diffraction peaks for the TiO_2 nanobelt film

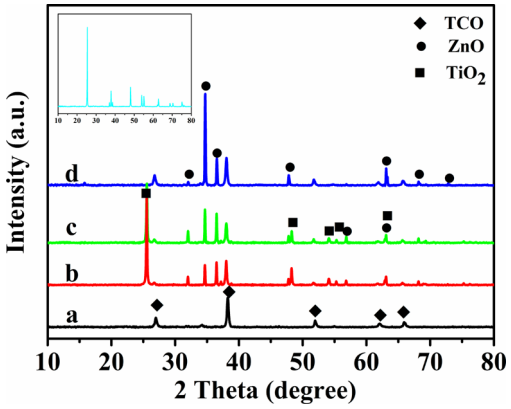

Figure 4. XRD patterns of the TCO substrate (a), flower-like TiO_2 nanobelt/ZnO nanorod film (b), grass-like TiO_2 nanobelt/ZnO nanorod film (c), and ZnO nanorod film (d). Inset is the XRD pattern of the TiO_2 nanobelt film.

around 2θ of 25.3°, 48.1°, 53.9°, 55.1°, and 62.8° correspond to (101), (200), (105), (211), and (204) planes of the anatase phase (JCPDS No. 21-1272), respectively (Figure 4, Inset). The characteristic diffraction peaks for the ZnO nanorod film around 2θ of 31.7°, 34.4°, 36.2°, 47.5°, 56.5°, 62.8°, 67.9°, and 72.5° correspond to the (100), (002), (101), (102), (110), (103), (112), and (004) planes of the wurtzite phase (JCPDS No. 36-1451), respectivley, and the characteristic peak at 34.4° has the maximal diffraction intensity. This indicates that the ZnO nanorod arrays grow mainly in the [0001] direction (Figure 4d). After the solution growth process, the flower-like and grass-like TiO_2 nanobelt/ZnO nanorod possess the diffraction peaks of anatase TiO_2 and wurtzite ZnO, simultaneously (Figure 4b, c), and both of the composites possess a high crystallinity.

3.2. Water Splitting Performance of the Hierarchical TiO_2 Nanobelt/ZnO Nanorod Structures. The water photoelectrolysis activity of the flower-like hierarchical TiO_2 nanobelt/ZnO nanorod photoelectrode was evaluated by measuring the photocurrent in 0.5 M Na_2SO_4 electrolyte under xenon lamp irradiance. By comparison, the ZnO nanorod and grass-like TiO_2 nanobelt/ZnO nanorod composite photoanodes were also measured. The dark scan curves of the above three samples have no photocurrent response with the increased potentials (Figure 5a). The flower-like hierarchical

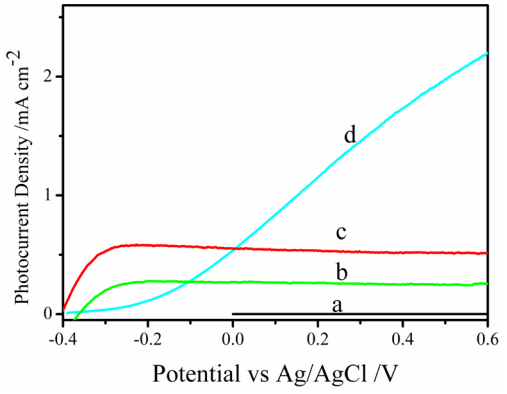

Figure 5. Dark scan curve of ZnO nanorod, grass-like, and flower-like TiO_2 nanobelt/ZnO nanorod photoelectrodes (a); photocurrent density/potential (J–V) curves of ZnO nanorod photoelectrode (b), grass-like TiO_2 nanobelt/ZnO nanorod photoelectrode (c), and flower-like TiO_2 nanobelt/ZnO nanorod photoelectrode (d) in 0.5 M Na_2SO_4 electrolyte under xenon lamp irradiance of 120 mW cm^{-2}. The scan rate was 10 mV s^{-1}.

TiO_2 nanobelt/ZnO nanorod heterogeneous nanostructure photoelectrodes (Figure 5d) generated a much higher photocurrent density than that of the grass-like TiO_2 nanobelt/ZnO nanorod composite (Figure 5c) and ZnO nanorod ones (Figure 5b) in the measured potential >0 V (vs Ag/AgCl) region. At a typical potential of +0.5 V (vs Ag/AgCl), the flower-like hierarchical TiO_2 nanobelt/ZnO nanorod photoelectrodes generated the highest stable photocurrent density of 1.90 mA cm^{-2} (Figure 6c), which improved ca. 760% and 380% compared with the ZnO nanorod and grass-like TiO_2 nanobelt/ZnO nanorod composite photoelectrode (0.25 and 0.51 mA cm^{-2}) (Figure 6a, b). Furthermore, the photocurrents of ZnO-based photoelectrodes at +0.5 V (vs Ag/AgCl) were able to decrease to zero when the xenon lamp irradiance was switched off. As soon as the xenon lamp irradiance was switched on again, the photocurrents almost recovered to the original values. After 30 min of xenon lamp irradiance, the photoelectrode still can possess the high photocurrent density. The photocurrent density only reduced ca. 5% after 20 min (Figure S1, Supporting Information). So, the ZnO-based photoelectrodes are stable during the xenon lamp irradiance.

3.3. Key Factors Determining the Water-Splitting Properties. It is conventionally believed that water-splitting properties of photoelectrodes are related to the UV–vis

dx.doi.org/10.1021/am402154k | ACS Appl. Mater. Interfaces 2013, 5, 8314–8320

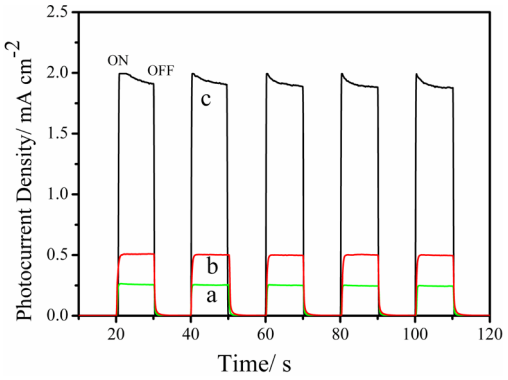

Figure 6. Typical photocurrent density/time (J–t) curves of the ZnO nanorod photoelectrode (a), grass-like TiO_2 nanobelt/ZnO nanorod photoelectrode (b), and flower-like TiO_2 nanobelt/ZnO nanorod photoelectrode (c) in 0.5 M Na_2SO_4 electrolyte when the xenon lamp irradiance was switched on (ON) and off (OFF) alternately. The working electrode potential was kept constant at 0.5 V vs Ag/AgCl.

absorption difference and photogenerated electron–hole separation efficiency. It can be seen that the light absorption difference between those photoelectrodes is indistinctive compared to photocurrent density difference (Figure 7). Due

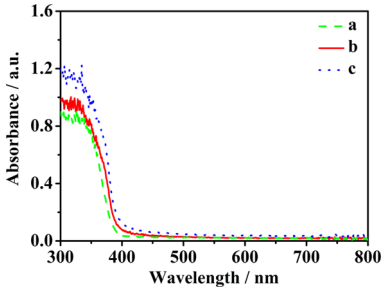

Figure 7. UV–vis absorption spectra of the ZnO nanorod (a), flower-like TiO_2 nanobelt/ZnO nanorod (b), and grass-like TiO_2 nanobelt/ZnO nanorod (c).

to the effect of one-dimensional morphology, the UV–vis spectra of the 1D TiO_2 nanobelt and the 1D ZnO nanorod have red-shifted compared to that of bulk ZnO, as previously reported,[25,50] and the UV–vis spectrum of the 1D TiO_2 nanobelt has lower Fermi energy level compared to the ZnO nanorod (Figure 7 and Figure S2, Supporting Information). So, the UV–vis absorption spectra of the flower-like and grass-like TiO_2 nanobelt/ZnO nanorod are red-shifted. The grass-like TiO_2 nanobelt/ZnO nanorod sample has the biggest light absorption, but the flower-like TiO_2 nanobelt/ZnO nanorod photoelectrode has the highest photocurrent density. So the light absorption difference is not the decisive factor for improved photocurrent density for the TiO_2 nanobelt/ZnO nanorod photoelectrode. The water-splitting properties of photoelectrodes are mainly related to the photogenerated electron–hole separation efficiency. KP-based SPV measurement is a good method to quantitatively study the surface work function change and photogenerated electron–hole separation.[51] According to the rule of the SPV generating process, for sub-band gap SPV, the sample absorbs photons of certain energy, and then the generated electron transfers either from surface states to the conduction band or from the valence band to surface states, yielding SPV response as long as electrons are separated from the holes. Relative to the Au reference probe, the ΔCPDs of the ZnO nanorod (Figure 8a), the grass-like TiO_2 nanobelt/ZnO nanorod (Figure 8b), and the flower-like

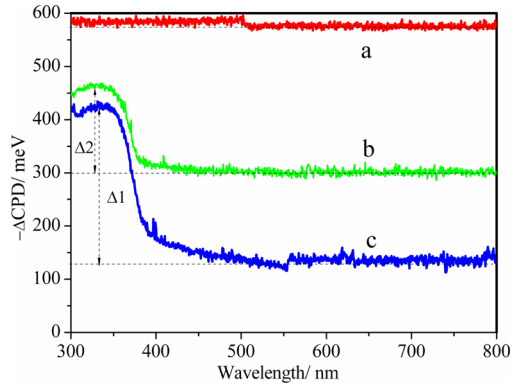

Figure 8. SPV spectra of the ZnO nanorod photoelectrode (a), grass-like TiO_2 nanobelt/ZnO nanorod composite photoelectrode (b), and flower-like TiO_2 nanobelt/ZnO nanorod heterogeneous photoelectrode (c) with illumination on top using the KP. Δ1: the response intensity of SPV for the flower-like TiO_2 nanobelt/ZnO nanorod heterogeneous photoelectrode. Δ2: the response intensity of SPV for the grass-like TiO_2/ZnO composite.

TiO_2 nanobelt/ZnO nanorod (Figure 8c) photoelectrodes are 0.56, 0.30, and 0.13 eV, respectively. Their work functions are 4.54 eV (φ_0), 4.80 eV (φ_2), and 4.97 eV (φ_1), respectively, and that of the Au probe is 5.1 eV (Scheme 1). It indicates that the

Scheme 1. Work Function and Energy Level Position of the ZnO Nanorod (a) and Grass-Like TiO_2 Nanobelt/ZnO Nanorod Composite and Flower-Like TiO_2 Nanobelt/ZnO Nanorod Heterogeneous Photoelectrode (b), Respectively[a]

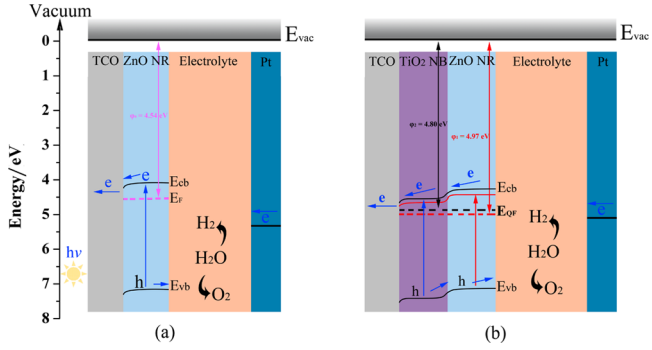

[a] E_{cb}, conduction band energy level; E_F, Fermi level; E_{vb}, valence band level; φ_0, the work function of the ZnO nanorod photoelectrode; φ_1, the work function of the flower-like TiO_2 nanobelt/ZnO nanorod heterogeneous photoelectrodes; φ_2, the work function of the grass-like TiO_2 nanobelt/ZnO nanorod photoelectrode.

flower-like TiO_2 nanobelt/ZnO nanorod nanostructure has the lowest quasi-Fermi energy level. The better electrical contact in this nanostructure effectively decreases the quasi-Fermi level compared with other photoelectrodes. This would favor a strong build-in field and contribute to photogenerated electron–hole separation. When the applied potential is below 0 V, it has the reversed electric field direction with the build-in field. So, the photogenerated electron–hole separation becomes more difficult for the flower-like TiO_2 nanobelt/ZnO nanorod photoelectrode. It has a decreased photocurrent density. When the applied potential is over 0 V, it has the

dx.doi.org/10.1021/am402154k | ACS Appl. Mater. Interfaces 2013, 5, 8314–8320

same electrical field direction as the built-in field, which results in the increased photogenerated electron−hole separation for the flower-like TiO_2 nanobelt/ZnO nanorod photoelectrode. So, it has the increased photocurrent density (Figure 5).

Furthermore, as the surfaces of grass-like and flower-like TiO_2 nanobelt/ZnO nanorod nanostructures were excited by xenon lamp irradiance from 800 to 300 nm, a steep decrease in surface work function was observed at ca. 450 nm which indicated the rise of surface potential and the appearance of positive SPV response (Figure 8). The response intensity of SPV for the flower-like TiO_2 nanobelt/ZnO nanorod heterogeneous nanostructure ($\Delta 1$) is larger than that of the grass-like TiO_2/ZnO composite ($\Delta 2$), which also proves that the flower-like TiO_2 nanobelt/ZnO nanorod heterogeneous nanostructure has higher photogenerated electron−hole separation efficiency. This is due to the novel structure morphology of flower-like TiO_2 nanobelt/ZnO nanorod heterogeneous architecture. When the composite absorbs photons of certain energy, the generated electrons and hole are separated. For the flower-like heterogeneous nanostructure, photoelectrons can quickly transfer from the TiO_2 nanobelt into the ZnO nanorod because TiO_2 nanobelts and ZnO nanorods have a better electrical contact. This would reduce the probability that the photoelectrons are recombined by the photogenerated holes (Scheme S1(a), Supporting Information). However, for grass-like nanostructure, most ZnO nanorods grow in the space between TiO_2 nanobelts, and only a few ZnO nanorods grow on the surface of TiO_2 nanobelts. This grass-like structure has a weaker electrical contant than the flower-like structure. So, photoelectrons transfer from the TiO_2 nanobelt into the ZnO nanorod is slower in grass-like structures. Much photogenerated electrons can only be detained in the TiO_2 nanobelt, which increased the possibility of recombination of electrons and holes (Scheme S1(b), Supporting Information). So, the photogenerated electron−hole separation efficiency for the flower-like heterogeneous nanostructure was enhanced compared to the grass-like nanostructure.

CONCLUSIONS

In this work, the flower-like TiO_2 nanobelt/ZnO nanorod photoelectrode has been fabricated via a facile solution growth routine. SEM and TEM images illustrate that flower-like ZnO nanorods are well dispersed orientationally on TiO_2 nanobelt films. At a typical potential of +0.5 V (vs Ag/AgCl), the flower-like hierarchical TiO_2 nanobelt/ZnO nanorod photoelectrode can yield a stable photocurrent density of 1.90 mA cm^{-2}, ca. 3.8 times as much as that of the grass-like composite. As evidenced by the surface photovoltage based on Kelvin probe, this improved performance is ascribed to the higher photogenerated electron−hole separation efficiency. In brief, the hierarchical and heterogeneous nanostructure photoelectrode possessed the effective photogenerated electron−hole separation efficiency, which resulted in higher photocurrent density.

ASSOCIATED CONTENT

Supporting Information

Figures S1 and S2 and Scheme S1. This material is available free of charge via the Internet at http://pubs.acs.org.

AUTHOR INFORMATION

Corresponding Author

*E-mail: kaipan@hlju.edu.cn. Tel.: +86 451 8660 9141. Fax: +86 451 8667 3647.

Notes

The authors declare no competing financial interest.

ACKNOWLEDGMENTS

We gratefully acknowledge the support of this research by the National Natural Science Foundation of China (21001042, 21101060, 51272070), the Program for New Century Excellent Talents in University (NCET-11-0958, NCET-11-0959), the Excellent Youth of Common Universities of Heilongjiang Province (1252G045), the Natural Science Foundation of Heilongjiang Province (B201003), Postdoctoral Research Foundation of Heilongjiang Province (LBH-Q11010, LBH-Q10018), and Program for Innovative Research Team in University (IRT-1237).

REFERENCES

(1) Lewis, N. S.; Nocera, D. G. *Proc. Natl. Acad. Sci.* **2006**, *103*, 15729−15735.
(2) lankenship, R. E.; Tiede, D. M.; Barber, J.; Brudvig, G. W.; Fleming, G.; Ghirardi, M.; Gunner, M. R.; Junge, W.; Kramer, D. M.; Melis, A.; Moore, T. A.; Moser, C. C.; Nocera, D. G.; Nozik, A. J.; Ort, D. R.; Parson, W. W.; Prince, R. C.; Sayre, R. T. *Science* **2011**, *332*, 805−809.
(3) Fujishima, A.; Honda, K. *Nature* **1972**, *238*, 37−38.
(4) O'Regan, B.; Grätzel, M. *Nature* **1991**, *353*, 737−739.
(5) Yang, X.; Wolcott, A.; Wang, G.; Sobo, A.; Fitzmorris, R. C.; Qian, F.; Zhang, J. Z.; Li, Y. *Nano Lett.* **2009**, *9*, 2331−2336.
(6) Park, H. G.; Holt, J. K. *Energy Environ. Sci.* **2010**, *3*, 1028−1036.
(7) Hagfeldt, A.; Grätzel, M. *Chem. Rev.* **1995**, *95*, 49−68.
(8) Kudo, A.; Miseki, Y. *Chem. Soc. Rev.* **2009**, *38*, 253−278.
(9) Jose, R.; Thavasi, V.; Ramakrishna, S. *J. Am. Ceram. Soc.* **2009**, *92*, 289−301.
(10) Chen, X.; Shen, S.; Guo, L.; Mao, S. *Chem. Rev.* **2010**, *110*, 6503−6570.
(11) Youngblood, W. J.; Lee, S.-H. A.; Maeda, K.; Mallouk, T. E. *Acc. Chem. Res.* **2009**, *42*, 1966−1973.
(12) Richter, C.; Menon, L. *Energy Environ. Sci.* **2010**, *3*, 427−433.
(13) Hartmann, P.; Lee, D.; Smarsly, B.; Janek, J. *ACS Nano* **2010**, *4*, 3147−3154.
(14) Wolcott, A.; Smith, W. A.; Kuykendall, T. R.; Zhao, Y.; Zhang, J. Z. *Adv. Funct. Mater.* **2009**, *19*, 1849−1856.
(15) Allam, N.; Shankar, K.; Grimes, C. *J. Mater. Chem.* **2008**, *18*, 2341−2348.
(16) Fujishima, A.; Kohayakawa, K.; Honda, K. *J. Electrochem. Soc.* **1975**, *122*, 1487−1489.
(17) Khan, S. U. M.; Al-Shahry, M.; Ingler, W. B., Jr. *Science* **2002**, *297*, 2243−2245.
(18) Hwang, Y. J.; Boukai, A.; Yang, P. *Nano Lett.* **2009**, *9*, 410−415.
(19) Mane, R.; Lee, W.; Pathan, H.; Han, S. *J. Phys. Chem. B* **2005**, *109*, 24254−24259.
(20) Hu, L.; Chen, G. *Nano Lett.* **2007**, *7*, 3249−3252.
(21) Tian, B.; Zheng, X.; Kempa, T. J.; Fang, Y.; Yu, N.; Yu, G.; Huang, J.; Lieber, C. M. *Nature* **2007**, *449*, 885−889.
(22) Chen, H. M.; Chen, C. K.; Chang, Y.-C.; Tsai, C.-W.; Liu, R.-S.; Hu, S.-F.; Chang, W.-S.; Chen, K.-H. *Angew. Chem., Int. Ed.* **2010**, *122*, 6102−6105.
(23) Park, J. H.; Kim, S.; Bard, A. J. *Nano Lett.* **2006**, *6*, 24−28.
(24) Yoon, K.; Cho, J.; Kang, D. *Mater. Res. Bull.* **1999**, *34*, 1451−1461.
(25) Chen, D.; Zhang, H.; Hu, S.; Li, J. *J. Phys. Chem. C* **2008**, *112*, 117−122.

(26) Wang, N.; Sun, C.; Zhao, Y.; Zhou, S.; Chen, P.; Jiang, L. *J. Mater. Chem.* **2008**, *18*, 3909−3911.
(27) Song, X.-M.; Wu, J.-M.; Tang, M.-Z.; Qi, B.; Yan, M. *J. Phys. Chem. C* **2008**, *112*, 19484−19492.
(28) Qiu, Y. C.; Yan, K. Y.; Deng, H.; Yang, S. H. *Nano Lett.* **2012**, *12*, 407−413.
(29) Mora-Sero, A.; Fabregat-Santiago, F.; Denier, B.; Bisquert, J.; Tena-Zaera, R.; Elias, J.; Levy-Clement, C. *Appl. Phys. Lett.* **2006**, *89*, 203117 (3 pages).
(30) Yin, Z. Y.; Wang, Z.; Du, Y. P.; Qi, X. Y.; Huang, Y. Z.; Xue, C.; Zhang, H. *Adv. Mater.* **2012**, *24*, 5374−5378.
(31) Liu, Z.; Zhang, Q.; Zhao, T.; Zhai, J.; Jiang, L. *J. Mater. Chem.* **2011**, *21*, 10354−10358.
(32) Zhu, K.; Neale, N. R.; Miedaner, A.; Frank, A. J. *Nano Lett.* **2007**, *7*, 69−74.
(33) Liu, Z.; Pesic, B.; Raja, K. S.; Rangarajua, R. R.; Misra, M. *Int. J. Hydrogen Energy* **2009**, *34*, 3250−3257.
(34) Rustomji, C.; Frandsen, C.; Jin, S.; Tauber, M. *J. Phys. Chem. B* **2010**, *114*, 14537−14543.
(35) Wang, G.; Wang, H.; Ling, Y.; Tang, Y.; Yang, X.; Fitzmorris, R.; Wang, C.; Zhang, J.; Li, Y. *Nano Lett.* **2011**, *11* (7), 3026−3033.
(36) Ling, Y.; Wang, G.; Reddy, J.; Wang, C.; Zhang, J.; Li, Y. *Angew. Chem., Int. Ed.* **2012**, *51*, 4074−4079.
(37) Hwang, Y.; Hahn, C.; Liu, B.; Yang, P. *ACS Nano* **2012**, *6* (6), 5060−5069.
(38) Cho, I. S.; Chen, Z.; Forman, A. J.; Kim, D. R.; Rao, P. M.; Jaramillo, T. F.; Zheng, X. *Nano Lett.* **2011**, *11*, 4978−4984.
(39) Wang, N.; Sun, C.; Zhao, Y.; Zhou, S.; Chen, P.; Jiang, L. *J. Mater. Chem.* **2008**, *18*, 3909−3911.
(40) Pan, K.; Dong, Y. Z.; Tian, C. G.; Zhou, W.; Tian, G. H.; Zhao, B. F.; Fu, H. G. *Electrochim. Acta* **2009**, *54*, 7350−7356.
(41) Tan, B.; Wu, Y. *J. Phys. Chem. B* **2006**, *110*, 15932−15938.
(42) Law, M.; Greene, L. E.; Johnson, J. C.; Saykally, R.; Yang, P. *Nat. Mater.* **2005**, *4*, 455−459.
(43) Zhao, Q. D.; Xie, T. F.; Peng, L. L.; Lin, Y. H.; Wang, P.; Peng, L.; Wang, D. J. *J. Phys. Chem. C* **2007**, *111*, 17136−17145.
(44) Zhao, Q. D.; Wang, D. J.; Peng, L. L.; Lin, Y. H.; Yang, M.; Xie, T. F. *Chem. Phys. Lett.* **2007**, *434*, 96−100.
(45) Chen, W.; Qiu, Y. C.; Yang, S. H. *Phys. Chem. Chem. Phys.* **2012**, *14*, 10872−10881.
(46) Yang, L.; Zhang, Y.; Ruan, W.; Zhao, B.; Xu, W.; Lombardi, J. R. *J. Raman Spectrosc.* **2010**, *41*, 721−726.
(47) Yang, Y.; Qu, L.; Dai, L.; Kang, T. S.; Durstock, M. *Adv. Mater.* **2007**, *19*, 1239−1243.
(48) Zhang, G. L.; Pan, K.; Zhou, W.; Qu, Y.; Pan, Q. J.; Jiang, B. J.; Tian, G. H.; Wang, G. F.; Xie, Y.; Dong, Y. Z.; Miao, X. H.; Tian, C. G. *Dalton Trans.* **2012**, *41*, 12683−12689.
(49) Zhu, H. C.; Iqbal, J.; Xu, H. J.; Yu, D. P. *J. Chem. Phys.* **2008**, *129*, 124713 (5 pages).
(50) Huang, M.; Wu, Y.; Feick, H.; Tran, N.; Weber, E.; Yang, P. *Adv. Mater.* **2001**, *13*, 113−116.
(51) Zhao, Q. D.; Yu, M.; Xie, T. F.; Peng, L. L.; Wang, P.; Wang, D. J. *Nanotechnology* **2008**, *19*, 245706(10pp).